Relativistic electron kinetic effects on laser diagnostics in burning plasmas

View the article online for updates and enhancements.

IOP ebooks™

Bringing you innovative digital publishing with leading voices to create your essential collection of books in STEM research.

Start exploring the collection - download the first chapter of every title for free.

Relativistic electron kinetic effects on laser diagnostics in burning plasmas

V.V. Mirnov[1] **and D.J. Den Hartog**

Department of Physics, University of Wisconsin-Madison,
1150 University Avenue, Madison, WI 53706, U.S.A.

E-mail: vvmirnov@wisc.edu

ABSTRACT: Toroidal interferometry/polarimetry (TIP), poloidal polarimetry (PoPola), and Thomson scattering systems (TS) are major optical diagnostics being designed and developed for ITER. Each of them relies upon a sophisticated quantitative understanding of the electron response to laser light propagating through a burning plasma. Review of the theoretical results for two different applications is presented: interferometry/polarimetry (I/P) and polarization of Thomson scattered light, unified by the importance of relativistic (quadratic in v_{Te}/c) electron kinetic effects. For I/P applications, rigorous analytical results are obtained perturbatively by expansion in powers of the small parameter $\tau = T_e/m_e c^2$, where T_e is electron temperature and m_e is electron rest mass. Experimental validation of the analytical models has been made by analyzing data of more than 1200 pulses collected from high-T_e JET discharges. Based on this validation the relativistic analytical expressions are included in the error analysis and design projects of the ITER TIP and PoPola systems. The polarization properties of incoherent Thomson scattered light are being examined as a method of T_e measurement relevant to ITER operational regimes. The theory is based on Stokes vector transformation and Mueller matrices formalism. The general approach is subdivided into frequency-integrated and frequency-resolved cases. For each of them, the exact analytical relativistic solutions are presented in the form of Mueller matrix elements averaged over the relativistic Maxwellian distribution function. New results related to the detailed verification of the frequency-resolved solutions are reported. The precise analytic expressions provide output much more rapidly than relativistic kinetic numerical codes allowing for direct real-time feedback control of ITER device operation.

KEYWORDS: Plasma diagnostics - interferometry, spectroscopy and imaging; Analysis and statistical methods

---

[1]Corresponding author.

Contents

1 Introduction

Toroidal interferometry/polarimetry (TIP) [1], poloidal polarimetry (PoPola) [2], and Thomson scattering systems (TS) [3] are major optical diagnostics being designed and developed for ITER. Each of them is based on the electron response to laser light propagating through the plasma. We examine the effects of relativistic electron thermal motion on the refractive indices and polarization of high-frequency electromagnetic waves (specifically laser light, both directed and scattered). Two different topics are covered: interferometry/polarimetry (I/P) and polarization of Thomson scattered light, unified by the importance of relativistic (quadratic in v_{Te}/c) electron kinetic effects. Fundamentally, each of these diagnostics relies upon a sophisticated quantitative understanding of the electron response to laser light propagating through a burning plasma. Improvements in this understanding are being used to guide and constrain the design of these diagnostics, and, once they are operational, will be used to improve measurement accuracy.

Interferometry and polarimetry are based on specific features of the plasma dielectric response. The magnetized plasma exhibits birefringence, and two orthogonal states of wave polarization with different refractive indices are present. Important consequences of plasma birefringence are the Faraday (FR) effect of rotation of the polarization plane and the Cotton-Mouton effect (CM) leading to both rotation and deformation of the polarization ellipse [4]. For many years, interpretaion of I/P measurements in plasma has been done using the cold plasma model. At high electron temperatures in fusion devices such as ITER, this will lead to significant errors. Rigorous analytical theory of the thermal corrections is developed perturbatively by expansion in powers of the small parameter $\tau = T_e/m_e c^2$, where T_e is electron temperature and m_e is electron rest mass [5]. There are two physically different sources of linear in τ corrections which are comparable in magnitude but contribute with opposite signs: non-relativistic (NR) Doppler-like effects and the relativistic

electron mass dependence on the velocity. The effects of finite electron temperature were addressed in the non-relativistic limit in ref. [6]. In ref. [5], it has been pointed out that both the NR effects and the relativistic electron mass factors are equally important for thermal corrections theory. The relativistic mass effect reduces the magnitude of the NR correction for the Cotton-Mouton effect and changes the signs of the corrections to the interferometric phase and Faraday rotation angle. The validity of the analytical results has been proven computationally by comparison with the ray-tracing numerical code GENRAY. Experimental validation of the analytical models has been made by analyzing data of more than 1200 pulses collected from high-T_e JET discharges [7]. Good agreement with the full relativistic model was demonstrated, and disagreement with the cold plasma and NR models. These were the first experimental observations of relativistic effects in plasma polarimetry. Based on the experimental validation the relativistic analytical expressions are included in the error analysis and design projects of the ITER TIP and PoPola systems [8]. The linear in τ model has been recently improved by adding quadratic in T_e corrections [9] and extended from Maxwellian to a more general class of anisotropic electron distributions to account for distortions caused by equilibrium current, ECRH and RF current drive effects [10, 11].

Interaction of the laser beam with plasma causes light to scatter away from the direction of the incident light. The power spectrum of this low intensity Thomson scattered light is routinely used for electron temperature measurement, with T_e proportional to the square of the scattered spectrum width [12]. Instead of frequency spectrum broadening, we analyze in this paper the polarization properties of TS radiation as a method of electron temperature measurement relevant to ITER operational regimes. The possibility of determining the plasma electron temperature by measuring the degree of depolarization was suggested in ref. [13]. If the dependence of the degree of depolarization on electron temperature is accurately known from theory, the accuracy of such a diagnostic could potentially exceed that of the conventional spectrum-based TS method. The theory is based on Stokes vector transformation and Mueller matrix method. This formalism was applied for the first time for Thomson scattering in ref. [14]. In our analysis, we followed ref. [14] with some important corrections and improvements. In particular, the finite transit time effect [15] is properly incorporated into the scattering operator. Another important improvement is optimal choice of the reference frame for averaging over velocity space. This allows derivation of exact relativistic analytical expressions for Mueller matrix elements averaged over the relativistic Maxwellian distribution function. The calculations are performed without any approximations for the full range of incident polarizations, scattering angles, and electron thermal motion from non-relativistic to ultra-relativistic. The general approach is subdivided into frequency-integrated and frequency-resolved applications. Solutions for the frequency-integrated case were obtained first and reported in a series of publications [10, 11, 16, 17]. Detailed theoretical description is presented in ref. [18]. Analytical solutions for the frequency-resolved case were obtained recently and published in a topical review [19] of the Thomson scattering polarization concept. The newly derived analytical solutions for the frequency-resolved case have been lately verified by comparison with the pure numerical code developed by L. Giudicotti and co-authors. The results are in a good agreement (< 0.01% deviations) verifying both calculations. Precise analytic expressions are important for burning plasmas where various techniques will be applied for direct real time feedback control of device operations with fast time resolution which is beyond the limits of slowly operating relativistic kinetic codes. The purpose of the present paper is to review already existing electron kinetic theory

results in support of optical diagnostics as well as to report new verification work confirming validity of the exact solutions for the frequency-resolved Mueller matrix elements. The progress achieved in Thomson scattering analysis is described first, followed by interferometry and polarimetry.

2 Polarization of Thomson scattering

Scattered electromagnetic waves are characterized not only by frequency but also by their polarization. The scattering process changes the polarization, an effect that becomes large in high-temperature burning plasmas. It has been typically described by the relativistic depolarization factor q (see refs. [4, 12]). When the scattered light collection system selects for a specific orientation of linear polarization, the factor q quantifies the reduction of the collected spectral intensity due to changes in the polarization of the incident linearly polarized laser light. The factor $q < 1$ arises from relativistic terms $\propto v_e^2/c^2$ in the polarization part of the scattering operator.

Although this reduction is referred to as depolarization, it is different from the use of depolarization considered in the present paper. Indeed, the aforementioned reduction of intensity takes place even for scattering on a single moving electron. In this case, the scattered electromagnetic wave has a Doppler-shifted frequency but still remains monochromatic and completely polarized. The transition from fully-polarized incident light to partially-polarized scattered light is caused by the superposition effect of a large number of randomly moving electrons. It results in broadening of the frequency spectrum and also renders the scattered radiation partially polarized even though the incident light is fully polarized. We focus our attention on this mechanism of loss of polarization in the process of incoherent TS.

The loss of polarization is quantified by the *degree of polarization P*, or equivalently by the *degree of depolarization $D = 1 - P$*. The polarization properties of a non-monochromatic plane wave are characterized by a 2×2 complex Hermitian coherency matrix $\hat{\mathbf{J}}$. The matrix is constructed from time averaged quadratic combinations of the field components and represented, in general, by four real quantities which can be equivalently expressed by four Stokes parameters or 4-component Stokes vector $\mathbf{S}$

$$\hat{\mathbf{J}} = \begin{pmatrix} <E_x E_x^\star> & <E_x E_y^\star> \\ <E_y E_x^\star> & <E_y E_y^\star> \end{pmatrix} = \frac{1}{2} \begin{pmatrix} S_0 + S_1 & S_2 + iS_3 \\ S_2 - iS_3 & S_0 - S_1 \end{pmatrix}. \tag{2.1}$$

The S_0 component is a measure of the total intensity I of the wave and the remaining components describe the polarization properties. For a purely monochromatic, fully polarized incident wave, the amplitudes and the phases of E_x and E_y are independent of time. In this case $\det|\hat{\mathbf{J}}| = 0$, leading to the relationship $S_0^2 = S_1^2 + S_2^2 + S_3^2$. Due to this connection between the components, the state of polarization of the incident laser light used in Thomson scattering systems, and the evolution of the polarization of monochromatic laser light used for interferometric/polarimetric diagnostics, is often described by the three-component unit Stokes vector $s_i = S_i/S_0$ ($i = 1, 2, 3$). This unit vector is characterized by the azimuth (orientation angle) of the polarization ellipse $0 \le \psi < \pi$ and the ellipticity angle $\chi = \pm \arctan(b_2/b_1)$ determined by the ratio of the minor and the major semi-axis ($-\pi/4 < \chi \le \pi/4$) (see figure 1). In section 2, we use the full four-component Stokes vector $\mathbf{S}^{(i)}$ to characterize monochromatic incident laser light with arbitrary elliptical polarization. Correspondingly, the four-component Stokes vector of fully polarized incident laser light is expressed as

$$\mathbf{S}^{(i)} = S_0^{(i)}(1, \ \cos 2\psi \cos 2\chi, \ \sin 2\psi \cos 2\chi, \ \sin 2\chi). \tag{2.2}$$

In section 3, the reduced three-component unit Stokes vector $\mathbf{s}$ is used.
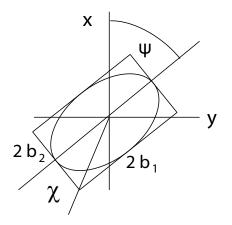
Figure 1. The azimuth of the polarization ellipse ψ (orientation angle) and the ellipticity angle χ for purely monochromatic, fully polarized incident wave.
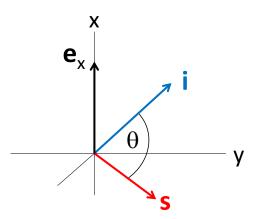

Figure 2. The incident and the scattered wave directions $\mathbf{i} = \mathbf{k}_i/|\mathbf{k}_i|$ and $\mathbf{s} = \mathbf{k}_s/|\mathbf{k}_s|$ (θ is the scattering angle in the plane perpendicular to the vector $\mathbf{e}_x = [\mathbf{s} \times \mathbf{i}]/\sin\theta$).

A fully unpolarized wave (natural light) is characterized by $S_1 = S_2 = S_3 = 0$. Any partially polarized wave can be decomposed into completely unpolarized and polarized portions. As they are statistically independent, the 4-component Stokes vector of the mixture is a sum of the respective vectors of the separate waves. Defining the unpolarized and polarized parts as $\mathbf{S}^{(\text{unpol})} = (S_0 - \sqrt{S_1^2 + S_2^2 + S_3^2}, 0, 0, 0)$ and $\mathbf{S}^{(\text{pol})} = (\sqrt{S_1^2 + S_2^2 + S_3^2}, S_1, S_2, S_3)$ yields the degrees of polarization and depolarization of the total wave field of intensity $I = S_0$. The degree of polarization is determined by the relative intensity I_{pol} of the polarized component

$$P = \frac{I_{\text{pol}}}{I} = \frac{\sqrt{S_1^2 + S_2^2 + S_3^2}}{S_0}, \quad D = 1 - P, \tag{2.3}$$

where $D = I_{\text{unpol}}/I$ is the degree of depolarization defined as the relative intensity of the unpolarized component. The degree of polarization P varies from the value $P = 0$ for unpolarized to $P = 1$ for fully polarized light.

2.1 Scattering from a single electron

Scattering from a single electron is treated as a re-emission of electromagnetic radiation by a free electron moving and oscillating in the electric and magnetic fields of the incident laser light. Instead of using the time-dependent scattered field $\mathbf{E}_s(\mathbf{r}, t)$ involved in the definition of the Stokes vector (2.1), we operate with the Fourier transformed truncated electric field $\mathbf{E}_s^{(T)}(\mathbf{r}, \omega)$. For a stationary incident laser beam characterized by an infinitely long wave packet of monochromatic radiation the truncation method is a substantial element of the Fourier transformation [18, 19]. The integration over t associated with the time averaging in (2.1) is converted to integration over ω. The integrand of this expression is defined as a spectral density of the Stokes vector $\mathbf{S}^{(s)}(\omega)$. Correspondingly, the full frequency integrated Stokes vector $\mathbf{S}^{(s)}$ is obtained by integrating the spectral density $\mathbf{S}^{(s)}(\omega)$ over the spectrum of the scattered radiation

$$\mathbf{S}^{(s)} = \int_{-\infty}^{+\infty} \mathbf{S}^{(s)}(\omega) d\omega. \tag{2.4}$$

We do not introduce additional indices to distinguish between frequency-integrated quantities such as $\mathbf{S}^{(s)}$ and frequency-dependent spectral density functions such as $\mathbf{S}^{(s)}(\omega)$, except for explicit indication of ω as an argument of all functions of the second type.

The most general method for the calculation of $\mathbf{S}^{(s)}(\omega)$ is based on the 4×4 Mueller matrix that describes the transformation of the Stokes vector, $\mathbf{S}^{(s)} = \hat{\mathbf{M}}^{(\text{single})}(\omega, \boldsymbol{\beta}) \cdot \mathbf{S}^{(i)}$, in the process of scattering on a single electron moving with an arbitrary velocity $\boldsymbol{\beta} = \mathbf{v}/c$. The specific form of the matrix is determined by the electric field components transformation. Using the Lienard-Wiechert potentials, the scattered electric field in the far-zone is expressed by an amplitude factor $f^{(T)}(\omega, \boldsymbol{\beta})$ and 2×2 matrix $\hat{\mathbf{\Pi}}$ which converts the incident field to the scattered field [18]). The spectral characteristic ω, the width T of the truncation interval and spatial dependence on the distance from the scattering volume to the point of observation (detector) are included in $f^{(T)}(\omega, \boldsymbol{\beta})$ while the explicit form of $\hat{\mathbf{\Pi}}$ is as follows

$$\begin{pmatrix} E_{sx}^{(T)}(\omega) \\ E_{st}^{(T)}(\omega) \end{pmatrix} = f^{(T)}(\omega, \boldsymbol{\beta}) \begin{pmatrix} a & b \\ -b & c \end{pmatrix} \begin{pmatrix} E_{ix} \\ E_{it} \end{pmatrix}, \qquad c = \beta_i + \beta_s + \beta_i \beta_s - \cos\theta - \frac{(\beta_i + \beta_s)^2}{1 + \cos\theta},$$

$$a = -(1 - \beta_i)(1 - \beta_s) + \beta_x^2(1 - \cos\theta), \quad b = \beta_x(1 + \cos\theta - \beta_i - \beta_s)\tan\frac{\theta}{2}. \qquad (2.5)$$

The matrix $\hat{\mathbf{\Pi}}$ consists of three elements a, b and c. They are functions of the velocity components $\beta_i = \boldsymbol{\beta} \cdot \mathbf{i}$, $\beta_s = \boldsymbol{\beta} \cdot \mathbf{s}$ along the wave propagation directions, $\beta_x = \boldsymbol{\beta} \cdot \mathbf{e}_x$ component orthogonal to the scattering plane and the scattering angle θ (see figure 2).

Using the scalar function $f^{(T)}(\omega, \boldsymbol{\beta})$ and matrix $\hat{\mathbf{\Pi}}$, the Stokes vector of the scattered wave is expressed in terms of quadratic combinations of the incident electric fields. This yields the Mueller matrix that can be conveniently expressed as a product $\hat{\mathbf{M}}^{(\text{single})}(\omega, \boldsymbol{\beta}) = C(\omega, \boldsymbol{\beta})\hat{\mathbf{W}}(\boldsymbol{\beta})$. The 4 x 4 matrix $\hat{\mathbf{W}}(\boldsymbol{\beta})$ is a function of quadratic combinations of the coefficients a, b and c

$$\hat{\mathbf{W}}(\boldsymbol{\beta}) = \begin{pmatrix} a^2 + 2b^2 + c^2 & a^2 - c^2 & 2b(a - c) & 0 \\ a^2 - c^2 & a^2 - 2b^2 + c^2 & 2b(a + c) & 0 \\ 2b(c - a) & -2b(a + c) & 2(ac - b^2) & 0 \\ 0 & 0 & 0 & 2(b^2 + ac) \end{pmatrix}. \qquad (2.6)$$

The scalar function $C(\omega, \boldsymbol{\beta})$ represents the square of the absolute value of $f^{(T)}(\omega, \boldsymbol{\beta})$. It is proportional to the δ-function that results from the limiting transition $T \to \infty$

$$C(\omega, \boldsymbol{\beta}) = \frac{r_0^2(1 - \beta^2)I^{(i)}}{2r^2(1 - \beta_s)^6}\delta\left(\omega - \omega_i\frac{1 - \beta_i}{1 - \beta_s}\right), \qquad (2.7)$$

where r_0, r are the classical electron radius and the distance from the scattering volume to the point of observation (detector), respectively. The normalization factor $S_0^{(i)} = I^{(i)}$, which determines the total intensity of the incident wave in equation (2.2) for $\mathbf{S}^{(i)}$ is removed from this expression and included in $C(\omega, \boldsymbol{\beta})$.

2.2 Frequency-integrated Mueller matrix

The Mueller matrix $\hat{\mathbf{M}}^{(\text{single})}(\omega, \boldsymbol{\beta})$ is used now to account for scattering from many electrons passing through the finite size scattering volume V. The scattering volume is defined by the

intersection of the region occupied by the laser beam and the region of observation determined by the collection optics. The equilibrium electron distribution function is defined as the number of electrons $dN = n_e f_M(\boldsymbol{\beta}) \, d\boldsymbol{\beta} \, d\mathbf{r}$ with velocities in the interval $\boldsymbol{\beta}$, $\boldsymbol{\beta} + d\boldsymbol{\beta}$ contained in a volume element $d\mathbf{r}$, where $f_M(\boldsymbol{\beta})$ is the relativistic Maxwellian distribution function normalized to unity

$$f_M(\boldsymbol{\beta}) = \frac{\mu \exp(-\mu/\sqrt{1 - \beta^2})}{4\pi K_2(\mu)(1 - \beta^2)^{5/2}}, \quad \mu = m_e c^2/T_e \tag{2.8}$$

and $K_2(\mu)$ is the modified Bessel function of the second kind [20]. An intuitive way of accounting for the effect of many electrons is to multiply the Mueller matrix from a single electron $\hat{\mathbf{M}}^{(\text{single})}(\omega, \boldsymbol{\beta})$ by the total number of electrons $n_e V f_M d\boldsymbol{\beta}$ in the scattering volume V. However, as it has been shown in original ref. [15] and discussed in detail in ref. [19], this intuitive approach fails to accurately characterize the scattered radiation due to the interruptive nature of the signals emitted from the finite scattering volume. This effect is referred in the literature as to the finite transit time effect (FTT). The FTT effect can be taken into account by using the corrected total number of electrons $(1 - \beta_s)n_e V f_M d\boldsymbol{\beta}$ for integration over the relativistic Maxwellian distribution function (2.8). Both $N = n_e V$ and $(1 - \beta_s)$ factors are missing in ref. [14].

The full frequency-integrated Stokes vector (2.4) is determined by the spectral Stokes vector density $\mathbf{S}^{(s)}(\omega, \boldsymbol{\beta})$ integrated over the entire frequency range. Using Mueller matrix representation gives $\mathbf{S}^{(s)}$ in the form of a product, $\mathbf{S}^{(s)} = \hat{\mathbf{M}}^{(\text{single})}(\boldsymbol{\beta}) \cdot \mathbf{S}^{(i)}$, where $\hat{\mathbf{M}}^{(\text{single})}(\boldsymbol{\beta})$ is the frequency-integrated Mueller matrix. Explicit integration over ω in (2.7) removes the δ-function and yields the frequency-integrated Mueller matrix in the form $\hat{\mathbf{M}}^{(\text{single})}(\boldsymbol{\beta}) = C(\boldsymbol{\beta})\hat{\mathbf{W}}(\boldsymbol{\beta})$ where $C(\boldsymbol{\beta}) = r_0^2 I^{(i)}(1 - \beta^2)/2r^2(1 - \beta_s)^6$. Adding the FTT correction factor $(1 - \beta_s)$, yields the final expression for the frequency-integrated Mueller matrix determined by the combined effect of many electrons

$$\hat{\mathbf{M}}(\mu, \theta) = \frac{r_0^2 N I^{(i)}}{2r^2} \int \frac{(1 - \beta^2) f_M(\boldsymbol{\beta}) d\boldsymbol{\beta}}{(1 - \beta_s)^5} \hat{\mathbf{W}}(\boldsymbol{\beta}). \tag{2.9}$$

For compact notation, we introduce the normalized dimensionless matrix $\hat{\mathbf{m}}(\mu, \theta) = \hat{\mathbf{M}}(\mu, \theta)/C_0$ where the dimensionless factor $C_0 = r_0^2 I^{(i)} N/2r^2$. The integration is performed in spherical coordinates with the β_z and β_x axes directed along $\mathbf{s}$ and $\mathbf{e}_x$, respectively. Four elements of the matrix $\hat{\mathbf{W}}$ are proportional to $b \propto \beta_x$. They are average to zero after integration over the velocity space. The remaining five elements are integrated in analytical form yielding functions of the scattering angle, $u = \cos\theta$, and electron temperature via the factor μ^2 and function $G(\mu) = K_1(\mu)/(\mu K_2(\mu))$, where K_1 and K_2 are modified Bessel functions of the second kind [20]

$$\begin{aligned}
m_{00} &= 1 + u^2 - 2G(\mu)(u^2 + 4u - 3) + (16/\mu^2)(1 - u)^2 \\
m_{01} &= m_{10} = 1 - u^2 \\
m_{11} &= 1 + u^2 + 2G(\mu)(u^2 - 4u + 1) + (12/\mu^2)(1 - u)^2 \\
m_{22} &= 2u - 4G(\mu)(u^2 - u + 1) - (12/\mu^2)(1 - u)^2 \\
m_{33} &= 2u - 4G(\mu)u(2u - 1) - (8/\mu^2)(1 - u)^2.
\end{aligned} \tag{2.10}$$

The details of the calculations are described in ref. [18]. Exact analytical solutions (2.10) are valid for the full range of scattering angles and electron thermal motion from non-relativistic to ultra-relativistic. The first terms in (2.10) describe the change of polarization in cold plasma ($\mu \to \infty$), the

second terms yield first order corrections in the weakly relativistic limit at $\mu \gg 1$, and the third terms dominate at ultra-relativistic temperatures $\mu \ll 1$. The use of the correct weighting factor $(1 - \beta_s)^{-5}$ in (2.9) is important. For example, the off-diagonal elements $m_{01} = m_{10}$ do not depend on electron temperature. Their temperature independence is a unique consequence of the fifth power weighting factor. The same integration performed for the sixth power weighting factor (without the FTT effect) or any other weighting factors would result in temperature-dependent off-diagonal elements.

The degree of depolarization (2.3) depends on T_e, θ, and polarization characteristics of the incident light ψ and χ. In spite of the large number of variables, the exact analytical results allow us to describe in a compact form the general properties of the degree of polarization. One particular example illustrating a maxima of D as a function of ψ and χ is shown in figure 3 for $T_e = 10$ keV and $\theta = 90°$. There is a peak of D at $\psi \simeq 82°$ for linear incident polarization but the absolute maximum is reached at $\psi = 90°$ for elliptically polarized light.

The ITER LIDAR TS system was planned to detect backscattered radiation at $\theta \sim 180°$. For such backscattered light, the degree of depolarization is quadratic in $T_e/m_e c^2 \ll 1$ and, therefore, small ($\sim 3 - 5\%$) at the temperatures expected in ITER. For a conventional TS system with $\theta \simeq 90°$, the situation is much more favorable with average $D \sim 20 - 25\%$. The cases of practical interest of circular and linear incident polarizations are illustrated in figure 4 at three scattering angles. Although circular incident polarization yields stronger depolarization of scattered radiation, rigorous minimization of the error bars shows that linear incident polarization is preferential for polarization-based diagnostics [17].
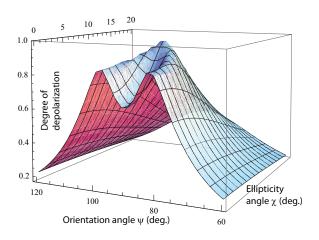

Figure 3. Depolarization degree vs orientation and ellipticity angles ψ and χ at $\theta = 90°$, $T_e = 10$ keV. There is a local maximum of D at $\psi \simeq 82°$ and $\chi = 0$ (linear polarization), but the absolute maximum is reached at $\psi = 90°$ and $\chi \simeq 9°$ (elliptical polarization).
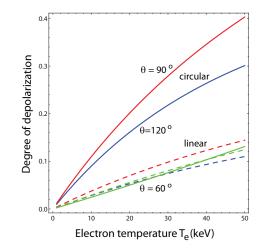

Figure 4. Depolarization degree vs T_e for three scattering angles: 60° (green), 90° (red) and 120° (blue) (solid lines: circular polarization at $\chi = 45°$; dashed lines: linear polarization at $\psi = \chi = 0$).

2.3 Frequency-resolved Mueller matrix

Realistic experimental constraints require detecting scattered photons within a limited wavelength range. This necessitates understanding the frequency-resolved degree of polarization first discussed

in ref. [14]. Rigorous analysis of polarization characteristics in a finite spectral band does not seem to be present in polarization literature. As suggested in ref. [18], some quantitative steps in this direction can be made on the basis of equation (2.4). Consider a partial contribution $\Delta \mathbf{S}^{(s)}$ to the spectrum integrated Stokes vector (2.4) from a narrow frequency interval $\Delta \omega$, such that $\Delta \mathbf{S}^{(s)} = \mathbf{S}^{(s)}(\omega) \Delta \omega$. Formal substitution of $\Delta \mathbf{S}^{(s)}$ to the equation (2.3) yields spectral degree of polarization $P(\omega)$ which is determined by the spectral density $\mathbf{S}^{(s)}(\omega)$ and does not depended on $\Delta \omega$

$$P(\omega) = \frac{\sqrt{S_1^{(s)^2}(\omega) + S_2^{(s)^2}(\omega) + S_3^{(s)^2}(\omega)}}{S_0^{(s)}(\omega)}. \quad (2.11)$$

The Stokes vector components $\mathbf{S}^{(s)}(\omega)$ are determined by the single electron spectral Mueller matrix (2.6), (2.7) averaged over the relativistic Maxwellian distribution function with the FTT correction factor $(1 - \beta_s)$

$$\hat{\mathbf{M}}(\omega, \mu, \theta) = \frac{r_0^2 n_e V E_0^2}{2 r^2} \int \frac{(1 - \beta^2) f_M(\boldsymbol{\beta}) d\boldsymbol{\beta}}{(1 - \beta_s)^5} \hat{\mathbf{W}}(\boldsymbol{\beta}) \delta \left(\omega - \omega_i \frac{1 - \beta_i}{1 - \beta_s} \right). \quad (2.12)$$

Contrary to the previous section 2.2, the integration over $\boldsymbol{\beta}$ is performed in (2.12) in a different co-ordinate system $(\mathbf{e}_x, \mathbf{e}_y, \mathbf{e}_z)$ with the z-axis directed along $\mathbf{k}_s - \mathbf{k}_i$ such that $\mathbf{e}_z = (\mathbf{k}_s - \mathbf{k}_i)/|\mathbf{k}_s - \mathbf{k}_i| = (\mathbf{s}(X + 1) - \mathbf{i})/k$, $\mathbf{e}_y = \mathbf{e}_z \times \mathbf{e}_x$, where $\mathbf{e}_x$ is the unit vector normal to the scattering plane. The dimensionless wave vector k and frequency shift X relative to the incident wave frequency are defined as

$$k = \frac{c|\mathbf{k}_s - \mathbf{k}_i|}{\omega_i} = \sqrt{X^2 + 2(X + 1)(1 - u)}, \quad X = \frac{\omega}{\omega_i} - 1. \quad (2.13)$$

The argument of the δ-function in (2.12) takes a form which allows for immediate integration over β_z: $\delta(\omega - \omega_i(1 - \beta_i)/(1 - \beta_s)) = (1 - \beta_s)\delta(\beta_\omega - \beta_z)/(\omega_i k)$, where $\beta_\omega = X/k$. Performing β_z-integration yields a double integral of two variables β_x and β_y over a circular area $\beta_x^2 + \beta_y^2 \leq 1 - \beta_\omega^2$ while the β_z component is fixed in the integrand, $\beta_z = \beta_\omega$. Four elements of the matrix $\hat{\mathbf{W}}$ are proportional to $b \propto \beta_x$ and averaged to zero after integration over β_x. The remaining five elements are integrated in the polar coordinate system $(\beta_\perp, \phi)$ such that $\beta_x = \beta_\perp \cos \phi$ and $\beta_y = \beta_\perp \sin \phi$ where $0 \leq \beta_\perp^2 \leq 1 - \beta_\omega^2$ and $0 \leq \phi \leq 2\pi$. The results for the dimensionless matrix $\hat{\mathbf{m}}(\omega, \mu, \theta) = \omega_i \hat{\mathbf{M}}(\omega, \mu, \theta)/C_0$ are presented in a compact form of a superposition of five well defined functions $E^{(n)}(p, r)$ with 25 coefficients, 13 of which are different non-zero rational functions of the dimensionless frequency X and scattering angle $u = \cos \theta$ given by equation (C12) in ref. [19]

$$\hat{\mathbf{m}}_{ij}(X, \mu, u) = \sum_{n=0}^{n=4} C_{ij}^{(n)}(X, u) E^{(n)}(p, r), \quad E^{(n)}(p, r) = \int_1^\infty \frac{dt \exp(-pt)}{(r^2 + t^2)^{(2n+1)/2}}, \quad n = 1, \ldots 4$$

$$E^{(0)}(p, r) = \exp(-p), \quad p = \mu \sqrt{\frac{X^2}{2(X + 1)(1 - u)} + 1}, \quad r^2 = \frac{2(X + 1)(1 + u)}{k^2}. \quad (2.14)$$

For backscattered radiation with $u = -1$ the argument $r = 0$. In this particular case, the integrals $E^{(n)}(p, r)$ coincide at $n = 1, \ldots 4$ with the exponential integral functions $E^{(n)}(p, 0) = E_{2n+1}(p)$ [20]).

The frequency-resolved degree of depolarization is defined as $D(\omega) = 1 - P(\omega)$ where $P(\omega)$ is given by (2.11). At given ω, the properties of $D(\omega)$ dependencies on T_e and θ are similar to those

presented in figures 3, 4 for the frequency-integrated Mueller matrix. The spectral dependence of $D(\omega)$ characterizes the sensitivity of the degree of depolarization to the frequency of the scattered radiation. In figure 5, typical examples of the spectral profiles $D(\omega)$ are shown at $T_e = 40$ keV and three scattering angles $\theta = 130°$, $150°$ and $180°$. At all angles, the functions $D(\omega)$ have maxima at the frequency approximately equal to the frequency of the incident wave. The peak values are about 15% higher than the degrees of depolarization shown by dashed lines and calculated at the same T_e and θ with the use of the frequency-integrated Mueller matrix. The right panel illustrates the dependence of the peak values $D(\omega_i)$ on incident polarization by plotting them along four boundaries of the polarization angles at $\theta = 130°$ (solid lines). The values of D determined from the frequency-integrated Mueller matrix are shown by dashed lines. Both solid and dashed curves demonstrate similar behavior but with slightly different amplitudes.
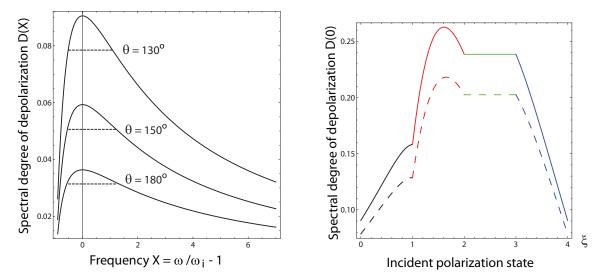

Figure 5. Left panel: spectral dependence of the degree of depolarization $D(X)$ for linear incident polarization with $\psi = 0$ at $\theta = 130°$, $150°$ and $180°$ (solid lines); the degree of depolarization at the same angles from the frequency-integrated Mueller matrix (dashed lines). The right panel: dependence of the peak values $D(0)$ on incident polarization along four boundaries of the polarization angles $0 \le \psi \le \pi/2$, $0 \le \chi \le \pi/4$ at $\theta = 130°$ (solid lines) [19]. The values of D for the frequency-integrated Mueller matrix are shown by dashed lines (all curves correspond to $T_e = 40$ keV).

2.4 Verification of the frequency-resolved solutions

Derivation of the newly obtained exact relativistic solutions (2.14) for the frequency-resolved Mueller matrix elements requires long analytical calculations. The final form of the solution is represented by the 5×5 matrix of the coefficients $C_{ij}^{(n)}$. The intermediate steps of the calculations are briefly described in the main part of ref. [19] while additional details are given in the appendix and in the supplementary material to the paper. The large amount of integrations and transformations in the derivation increases the probability of mistakes in the final analytical expressions. Partial verification of the results was performed in ref. [19] numerically by integrating (2.14) over the entire frequency interval $-1 \le X \le \infty$ and comparing with the frequency-integrated quantities (2.10). The correctness of the analytical calculations was also confirmed by evaluating the spectral power

$<|E_x|^2>(X) = (S_0^{(s)} + S_1^{(s)})/2 \propto (m_{00} + m_{11} + 2m_{01})/2$ along the direction $\mathbf{e}_x$ normal to the scattering plane (see figure 2) and comparing it with the exact relativistic spectral power [21] obtained for linear incident polarization perpendicular to the scattering plane ($\psi = \chi = 0$). Although these two benchmarks were successful they cannot guarantee the accuracy of all five Mueller matrix elements and confirm validity of the exact analytical solutions. Because of the importance of this question soon after publication of ref. [19] the solutions became a subject of a thorough verification by the Italian group headed by Prof. L. Giudicotti. The purpose of their work was to benchmark the expressions (2.14) with the purely numerical 3D integration code independently developed by this group for TS polarization analysis [22]. The main steps and results of the verification are decribed below.

Originally, the feasibility of the frequency-resolved TS polarimetry and an expression similar to (2.12) but with incorrect sixth power weighting factor $(1 - \beta_s)^{-6}$ were suggested in ref. [14]. Two angular characteristics $\eta_1 = \beta_i/\beta$ and $\eta_2 = \beta_s/\beta$ and the variable $\beta = |\boldsymbol{\beta}|$ were suggested as the variables of integration over the velocity space. They are substantially different from the variables of integration used in section 2.3. In these variables the volume element in the velocity space becomes [14]

$$d\beta_x d\beta_y d\beta_z = \frac{\beta^2 d\beta d\eta_1 d\eta_2}{4\pi \sqrt{W}}, \quad W = \sin^2 \theta - \eta_1^2 - \eta_2^2 + 2\eta_1 \eta_2 \cos \theta \qquad (2.15)$$

The set of variables (2.15) was used by the Italian group for the development of a pure numerical 3D integration code with correct fifth power weighting factor (see equation (2.12)). After integration of the delta-function over one of the angular variables, the other two integrations are performed numerically with the use of a 2D computational grid. This procedure yields the numerical functional dependencies of all five Mueller matrix elements $m_{ij}^{(\text{num})}$ on the dimensionless wavelength $\Lambda = \lambda/\lambda_i - 1$, u and T_e [23]. These dependencies are compared with the analytical expressions (2.14) referred further to as $m_{ij}^{(\text{an})}$. The analytical expressions are evaluated for the same arguments (grid points) as the numerical functions $m_{ij}^{(\text{num})}$. For this purpose, the analytical solutions (2.14) are transformed from the frequency X to the wavelength variable Λ and are multiplied by the factor $(1 + \Lambda)^{-2}$ to take into account a relationship between the differentials $dX = -d\Lambda/(1 + \Lambda)^2$. The use of the different variables of integration and the integration methods makes both numerical and analytical approaches fully independent providing a good basis for rigorous benchmarking.

The measure of disagreement between analytical and numerical results is determined by their relative deviations $R_{ij}(\Lambda, u, T_e) = |(m_{ij}^{(\text{an})} - m_{ij}^{(\text{num})})/m_{ij}^{(\text{an})}|$. To illustrate the results of the verification these quantities are plotted as functions of Λ in figure 6 for five Mueller matrix elements evaluated at $\theta = 140°$ and $T_e = 25$ keV which are typical for the ITER conventional core TS system. A complete scan and analysis of the full parameter space requires a large amount of computation and will be published in a separate paper. The analytical and numerical results are in excellent agreement ($< 0.01\%$ deviation), verifying both methods. This successful cross-check of the analytical solutions for all five Mueller matrix elements encourages use of them as a reliable and universal tool for general description of the spectral and polarization properties of incoherent Thomson scattering. Analytical evaluation of the $m_{ij}^{(\text{an})}$ functions at 100 equidistant points within the interval $-0.2 < \Lambda < 1$ takes about 77 ms on a standard laptop PC while the same data calculated numerically require a CPU time about two orders of magnitude longer. This leads to an important conclusion that exact analytical
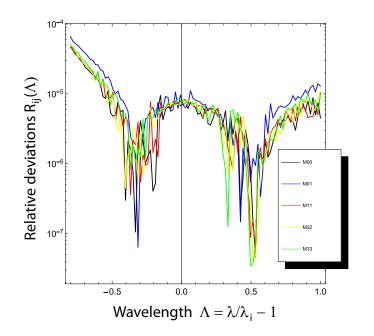
Figure 6. Plots of $R_{ij}(\Lambda)$ vs Λ evaluated at 100 equidistant points within the interval $-0.2 \leq \Lambda \leq 1$ at $\theta = 140°$, $T_e = 25\,\text{keV}$ for five frequency-resolved Mueller matrix elements. The analytical and numerical results are in excellent agreement.

solutions can be effectively used for direct real time TS polarization measurements in ITER with fast time resolution which is beyond the capability of numerical codes.

3 Interferometry and polarimetry

The ITER TIP system is designed for tangential plasma density measurement from both traditional interferometry and Faraday-effect polarimetry (by both direct measurement and as a means to compensate fringe jumps appearing in the interferometer). It is based on the use of laser beams with the wavelengths 10.6/5.3 μ*m* propagating along five chords in the toroidal plane which are double-passed by retro-reflection from corner cube reflectors mounted in the ITER walls. In a cold plasma, the interferometric phase Φ and the Faraday rotation angle of polarization ψ_F are proportional to the line integral of the electron density and the line integral of the electron density multiplied by the parallel component of the magnetic field, respectively. For the ITER TIP system parameters, $n \simeq 10^{20}\,m^{-3}$, $B_\parallel \simeq 5.3\,T$, $L \simeq 21\,m$, $\lambda = 10.6\,μm$, they are as follows

$$\Phi^{(\text{cold})}[rad] = 2.82 \times 10^{-21} \lambda[μm] \int n_e(z)[m^{-3}]dz[m] \simeq 63, \tag{3.1}$$

$$\psi_F^{(\text{cold})}[rad] = 2.62 \times 10^{-25} \lambda^2[μm] \int n_e(z)[m^{-3}]B_\parallel(z)[T]dz[m] \simeq 0.33. \tag{3.2}$$

The ITER PoPola diagnostic is based on the Faraday (FR) and Cotton-Mouton (CM) effects and provides a unique method for internal magnetic field and current profile measurements as well as electron density. It is anticipated to operate with long wavelength far-infrared laser beams (118/50 μ*m*) propagating in the poloidal plane along nine chords via an equatorial port and six

chords via an upper port. In this case, with propagation largely perpendicular to the magnetic field, the Cotton-Mouton effect becomes significant and leads to a change in the ellipticity characterized by the ellipticity angle χ. For the PoPola system parameters, $n \simeq 10^{20}\,m^{-3}$, $B_\perp \simeq 5.3\,T$, $L \simeq 8\,m$, $\lambda = 118\,\mu m$, the induced ellipticity of radiation initially linearly polarized at 45^0 to $\mathbf{B}_\perp$ is given by

$$\chi^{(\text{cold})}[rad] = 2.46 \times 10^{-29} \lambda^3[\mu m] \int n_e(z)[m^{-3}] B_\perp^2(z)[T] dz[m] \simeq 0.91. \tag{3.3}$$

3.1 Thermal correction for Maxwellian electrons

One source of error is finite electron temperature effects neglected in the cold plasma dispersion relation. Thermal corrections are proportional to $\tau = T_e/m_e c^2$ and are small at $T_e \sim 1\,\text{keV}$, but become sizable at $T_e \geq 10\,\text{keV}$. The effects caused by the relativistic electron mass dependence on the velocity are opposite compared to the non-relativistic (NR) Doppler-like contributions. They change the sign of the NR thermal corrections for the interferometric phase and Faraday rotation angle, and reduce the magnitude of the NR correction for the Cotton-Mouton effect. At $T_e = 25\,\text{keV}$, the resulting values of these quantities relative to their values in cold plasma are, respectively, $-7.5\%, -10\%$ and $+22.5\%$ (see ref. [5]), while the non-relativistic model [6] yields overestimated values, $+5\%, +15\%$ and $+60\%$, correspondingly.

For formal analysis of the problem an iterative technique for solving the relativistic Vlasov kinetic equation was developed in ref. [5]. The key element of the method is expansion in powers of $Y = \omega_{ce}/\omega \ll 1$ instead of integration over azimuthal angle in the velocity space. This avoids the use of a complicated Bessel function series representation. Instead, expansion is performed by successive differentiations of simple standard trigonometric functions. This leads to the result in the analytic form of a double power series expansion of the dielectric tensor ϵ'_{ij} in $Y \ll 1$ and $\tau \ll 1$ to any desirable order. Six iterations are enough to obtain the dielectric tensor expanded to second order in τ with all relativistic factors taken into account. Initially, the results are obtained in the reference frame with the z'-axis oriented along $\mathbf{B}_0$ and the $\mathbf{k}$ vector in the x', z' plane with the angle α between them. Then, the dielectric tensor is transfered to the laboratory reference frame x, y, z with the z-axis oriented along $\mathbf{k}$ while $\mathbf{B}_0$ is arbitrary and has the Cartesian coordinates $B_0(\sin\alpha\cos\beta, \sin\alpha\sin\beta, \cos\alpha)$. Finally, expressing E_z in terms of E_x and E_y yields two coupled equations for E_x and E_y (Jones equations)

$$\begin{pmatrix} N^2 - \eta_{xx} & -\eta_{xy} \\ -\eta_{yx} & N^2 - \eta_{yy} \end{pmatrix} \begin{pmatrix} E_x \\ E_y \end{pmatrix} = 0, \quad \eta_{ij} = \epsilon_{ij} - \epsilon_{iz}\epsilon_{zj}/\epsilon_{zz}, \quad i, j = 1, 2. \tag{3.4}$$

In the WKB approximation, the electric field of the wave is characterized by the slowly varying complex amplitude $\mathbf{E}$. The model which adequately describes evolution of polarization of the wave in a nonuniform plasma and magnetic field is based on the Stokes vector equation

$$\frac{d\mathbf{s}}{dz} = \mathbf{\Omega} \times \mathbf{s}, \tag{3.5}$$

where the three-component unit Stokes vector $\mathbf{s}$ is defined in section 2, z is a coordinate along the propagation direction and the spatially varying angular velocity vector $\mathbf{\Omega}(z) = (\omega/2c)(\eta_{xx} - \eta_{yy}, 2\mathcal{R}e\{\eta_{xy}\}, 2\mathcal{I}m\{\eta_{xy}\})$. The basic equation (3.5) allows us to address the issue of the coupling

between the FR and the CM effects while properly accounting for the thermal effects. The Ω_1 and Ω_2 components are responsible for the CM effect and Ω_3 describes the Faraday rotation. Linear in τ temperature corrections were incorporated in this model in ref. [5]. The precision of this lowest-order linear in τ model may be insufficient; using the same iterative technique a more sophisticated model with τ^2-order corrections was developed in ref. [9] to satisfy the accuracy requirements for the ITER TIP and PoPola systems. The expression for $\boldsymbol{\Omega}$ that combines all three contributions reads

$$\boldsymbol{\Omega} = \boldsymbol{\Omega}^{(c)} + \frac{T_e}{m_e c^2} \begin{pmatrix} 9\Omega_1^{(c)}/2 \\ 9\Omega_2^{(c)}/2 \\ -2\Omega_3^{(c)} \end{pmatrix} + \left(\frac{T_e}{m_e c^2} \right)^2 \begin{pmatrix} 15\Omega_1^{(c)}/8 \\ 15\Omega_2^{(c)}/8 \\ 3\Omega_3^{(c)} \end{pmatrix}, \ \boldsymbol{\Omega}^{(c)} = \frac{\omega}{2c} \begin{pmatrix} ZY^2 \sin^2 \alpha \cos 2\beta \\ ZY^2 \sin^2 \alpha \sin 2\beta \\ 2ZY \cos \alpha \end{pmatrix}, \quad (3.6)$$

where $Z = \omega_{pe}^2/\omega^2 \ll 1$. Relative deviation of the interferometric phase Φ from its cold plasma value $\Phi^{(\text{cold})}$ is caused by the thermal effects and reads

$$\frac{\Delta\Phi}{\Phi^{(\text{cold})}} = \left(-\frac{3}{2} \int \frac{n_e T_e}{m_e c^2} dz + \frac{15}{8} \int \frac{n_e T_e^2}{m_e^2 c^4} dz \right) / \int n_e dz. \quad (3.7)$$

For the ITER TIP system with a CO_2 laser at $\lambda = 10.6$ μm and $T_e = 25$ keV, the linear thermal correction to the interferometric phase is large ($\sim 270°$), and the quadratic correction is also significant ($\sim 17°$).

3.2 Non-Maxwellian electron distribution function

New effects come into play when the electron distribution function develops an anisotropy. This could be caused by a large mean electron drift velocity $U_{\|e}$ (parallel equilibrium current), an enhanced effective perpendicular temperature $T_\perp$ in ECRH heated plasmas, or a large effective parallel temperature $T_\|$ due to LH current drive. The corresponding vector $\boldsymbol{\Omega}$ in the Stokes equation is presented as a sum of three contributions $\boldsymbol{\Omega} = \boldsymbol{\Omega}^{(0)} + \boldsymbol{\Omega}^{(B)} + \boldsymbol{\Omega}^{(U)}$. The first term does not depend on the magnetic field and describes the effect of birefringence caused by the temperature anisotropy

$$\boldsymbol{\Omega}^{(0)} = (1 - N^2) \frac{\omega Z}{2c} \frac{(T_\| - T_\perp)}{m_e c^2} \begin{pmatrix} 1 \\ 1 \\ 0 \end{pmatrix} \propto \frac{\omega Z^2}{2c} \frac{(T_\| - T_\perp)}{m_e c^2}. \quad (3.8)$$

It results in evolution of the polarization ellipse similar to the usual "magnetic" Cotton-Mouton effect. The magnitude of the effect is strongly reduced by almost exact cancellation of the relativistic and non-relativistic Doppler-like contributions expressed, correspondingly, by the unity and N^2 term in the factor $(1 - N^2)$.

The second term, $\boldsymbol{\Omega}^{(B)}$, describes the generalization of linear in τ isotropic results to the case of non-Maxwellian anisotropic distributions. It is important for correction of the interpretation errors in plasmas with non-Maxwellian distributions generated by ECRH and other RF sources such as EC and LH current drive

$$\boldsymbol{\Omega}^{(B)} = \boldsymbol{\Omega}^{(c)} + \cos 2\alpha \frac{(T_\| - T_\perp)}{2m_e c^2} \begin{pmatrix} 10\Omega_1^{(c)} \\ 10\Omega_2^{(c)} \\ 3\Omega_3^{(c)} \end{pmatrix} + \left(\frac{1}{2m_e c^2} \right) \begin{pmatrix} (5T_\| + 4T_\perp)\Omega_1^{(c)} \\ (5T_\| + 4T_\perp)\Omega_2^{(c)} \\ -(3T_\| + T_\perp)\Omega_3^{(c)} \end{pmatrix}. \quad (3.9)$$

The third term, $\mathbf{\Omega}^{(U)}$, describes evolution of polarization due to non-zero mean electron drift velocity $U_{\parallel e}$ (equilibrium current)

$$\mathbf{\Omega}^{(U)} = \frac{\omega U_{\parallel e}}{c^2} \begin{pmatrix} ZY^2 \cos\alpha \sin^2\alpha \cos 2\beta \\ ZY^2 \cos\alpha \sin^2\alpha \sin 2\beta \\ ZY \cos 2\alpha \end{pmatrix}. \tag{3.10}$$

Motion of the electron component as a whole can be considered as the Fizeau effect, that is, the phase velocity of electromagnetic waves depends on whether they propagate in a moving or stationary medium. In cold non-magnetized plasma, the interferometric phase is insensitive to $U_{\parallel e}$ because of exact cancelation of the Fizeau effect due to specific scaling of plasma refractive index on frequency, $N^2 = 1 - \omega_{pe}^2/\omega^2$. In the presence of a magnetic field, the non-magnetized electron dispersion relation is modified. This eliminates the effect of cancellation and leads to evolution of the wave polarization caused by the combined action of the magnetic field and electron drift velocity and described by the Stokes vector equation with the vector $\mathbf{\Omega}^{(U)}$. This may open new possibilities for diagnosis or measurements of the parallel equilibrium current (Fizeau interferometry/polarimetry).

4 Summary

The present overview is focused on the progress achieved during the last two decades in theoretical support for polarization-based TS diagnostics and interferometry/polarimetry in high-T_e plasmas. For the TS applications, the general formalism of the Mueller matrix and Stokes vectors is subdivided into the frequency-integrated and frequency-resolved limiting cases. For both of them, exact fully relativistic analytical solutions are obtained. They form a basis for the analysis and optimization of the polarization-based TS schemes as well as for the analysis of an intermediate situation when the optical instrumentation has a finite wavelength band.

Newly obtained relativistic expressions for the frequency resolved Mueller matrix are verified by integrating over the entire frequency interval and comparing with the frequency-integrated quantities. The correctness is also confirmed by checking consistency with exact relativistic spectral power results [21]. The frequency-resolved solutions have been also verified by comparison with the pure numerical code developed by L. Giudicotti and co-authors. The results are in a good agreement (< 0.01% deviations) verifying both calculations. Precise analytic expressions are important for direct real time feedback control of device operations with fast time resolution which is beyond the capability of relativistic kinetic codes.

There are a large number of publications describing the optimization of potential polarization-based TS diagnostic capabilities. Different modifications are compared, searching for the variant with the smallest experimental error bars [17]. Generally, forward scattering at $\theta < 90°$ is more favorable for polarization-based TS diagnosis than backscattering at the complementary angle $180° - \theta$. In this sense, the planned ITER core TS system geometry with predominantly backward scattered collection optics is not optimal for polarization-based diagnosis. For the ITER core TS system, combinations of polarization-based and spectral-based techniques are discussed, including the hybrid method suggested recently by L. Giudicotti and co-authors [24]. In addition to the ITER core TS application there are a number of other opportunities for implementing polarization-based Thomson scattering diagnostics. Although these methods have not yet been fully investigated in experiments,

an attempt to measure the depolarisation effect has recently been performed on JET. In addition to JET, an experiment to measure the depolarization of the TS radiation has been proposed on the Frascati Tokamak Upgrade (FTU). This information as well as a possible experimental test of a polarimetric Thomson scattering diagnostic technique on the W7-X stellarator are briefly discussed in ref. [19].

Acknowledgments

References

[1] M.A. Van Zeeland et al., *Conceptual design of the tangentially viewing combined interferometer-polarimeter for ITER density measurements*, *Rev. Sci. Instrum.* **84** (2013) 043501.

[2] R. Imazawa et al., *A new approach of equilibrium reconstruction for ITER*, *Nucl. Fusion* **51** (2011) 113022.

[3] M. Bassan et al., *Thomson scattering diagnostic systems in ITER*, 2016 *JINST* **11** C01052.

[4] I.H. Hutchinson, *Principles of plasma diagnostics*, Cambridge University Press, Cambridge U.K., (2002), pg. 440.

[5] V.V. Mirnov et al., *Finite electron temperature effects on interferometric and polarimetric measurements in fusion plasmas*, *Phys. Plasmas* **14** (2007) 102105.

[6] S.E. Segre and V. Zanza, *Finite electron temperature effects in plasma polarimetry and interferometry*, *Phys. Plasmas* **9** (2002) 2919.

[7] O.P. Ford et al., *Experimental verification of relativistic finite temperature polarimetry effects at JET*, *Plasma Phys. Control. Fusion* **51** (2009) 065004.

[8] M.A. Van Zeeland et al., *Tests of a CO_2 and quantum cascade laser based two-color interferometer and polarimeter for ITER density measurements*, *Plasma Phys. Control. Fusion* **59** (2017) 125005.

[9] V.V. Mirnov et al., *Electron kinetic effects on interferometry and polarimetry in high temperature fusion plasmas*, *Nucl. Fusion* **53** (2013) 113005.

[10] V.V. Mirnov et al., *Electron kinetic effects on interferometry, polarimetry and Thomson scattering measurements in burning plasmas*, *Rev. Sci. Instrum.* **85** (2014) 11D302.

[11] V.V. Mirnov et al., *Electron kinetic effects on optical diagnostics in fusion plasmas*, in *Fusion Reactor Diagnostics*, Varenna Italy, 9–13 September 2013 [*AIP Conf. Proc.* **1612** (2015) 157].

[12] J. Sheffield et al., *Plasma scattering of electromagnetic radiation*, 2nd ed., Academic Press, U.S.A., (2011).

[13] F. Orsitto and N. Tartoni, *Proposal for a new electron temperature diagnostic for fusion reactors*, *Rev. Sci. Instrum.* **70** (1999) 798.

[14] S.E. Segre and V. Zanza, *Polarization of radiation in incoherent Thomson scattering by high temperature plasma*, *Phys. Plasmas* **7** (2000) 2677.

[15] R.E. Pechacek and A.W. Trivelpiece, *Electromagnetic wave scattering from a high-temperature plasma*, *Phys. Fluids* **10** (1967) 1688.

[16] V.V. Mirnov et al., *Electron kinetic effects on interferometry, polarimetry and Thomson scattering measurements in burning plasmas*, in *Proc. IAEA Fusion Energy Conf., ITR/P5-32, San Diego CA U.S.A.,* 8–13 *October* 2012, IAEA, Vienna Austria, (2013), pg. 604.

[17] E. Parke et al., *A polarization-based Thomson scattering technique for burning plasmas*, in *Proceedings of the* 16th *International Symposium on Laser-Aided Plasma Diagnostics*, Madison WI U.S.A., (2013) [2014 *JINST* **9** C02030].

[18] V.V. Mirnov et al., *Exact relativistic expressions for polarization of incoherent Thomson scattering*, *Phys. Plasmas* **23** (2016) 052108.

[19] V.V. Mirnov and D.J. Den Hartog, *Topical review: polarization of incoherent Thomson scattering for electron temperature measurement*, *Plasma Phys. Control. Fusion* **59** (2017) 063001.

[20] M. Abramowitz and I.A. Stegun, *Handbook of mathematical functions*, U.S. Department of Commerce, Nat. Bureau of Standards, Washington D.C. U.S.A., (1964).

[21] O. Naito et al., *Analytic formula for fully relativistic Thomson scattering spectrum*, *Phys. Fluids* **B 5** (1993) 4256.

[22] L. Giudicotti, *Polarimetric Thomson scattering for high T_e fusion plasmas*, 2017 *JINST* **12** C11002.

[23] L. Giudicotti, private communication, (2017).

[24] L. Giudicotti et al., *Conceptual design of a polarimetric Thomson scattering diagnostic in ITER*, 2016 *JINST* **11** C01071.